JOURNAL OF APPLIED CRYSTALLOGRAPHY

ISSN: 1600-5767
journals.iucr.org/j

Effects of magnetic and non-magnetic doping on the vortex lattice in MgB_2

Elizabeth R. Louden, Soham Manni, Judah E. Van Zandt, Allan W. D. Leishman, Valentin Taufour, Sergey L. Bud'ko, Lisa DeBeer-Schmitt, Dirk Honecker, Charles D. Dewhurst, Paul C. Canfield and Morten R. Eskildsen

J. Appl. Cryst. (2022). **55**, 693–701

JOURNAL OF APPLIED CRYSTALLOGRAPHY

ISSN 1600-5767

Effects of magnetic and non-magnetic doping on the vortex lattice in MgB_2[1]

Elizabeth R. Louden,[a] Soham Manni,[b]‡ Judah E. Van Zandt,[a] Allan W. D. Leishman,[a] Valentin Taufour,[b,c]§ Sergey L. Bud'ko,[b,c] Lisa DeBeer-Schmitt,[d] Dirk Honecker,[e] Charles D. Dewhurst,[e] Paul C. Canfield[b,d] and Morten R. Eskildsen[a]*

[a]Department of Physics, University of Notre Dame, Notre Dame, IN 46556, USA, [b]Department of Physics and Astronomy, Iowa State University, Ames, IA 50011, USA, [c]Division of Materials Science and Engineering, Ames Laboratory, Ames, IA 50011, USA, [d]Large Scale Structures Group, Neutron Sciences Directorate, Oak Ridge National Laboratory, Oak Ridge, TN 37831, USA, and [e]Institut Laue–Langevin, 71 avenue des Martyrs, CS 20156, F-38042 Grenoble Cedex 9, France. *Correspondence e-mail: eskildsen@nd.edu S. Mühlbauer,, Technical University of Munich, Germany

Received 22 February 2022
Accepted 2 May 2022

Edited by S. Mühlbauer, Technical University of Munich, Germany

[1] This article is part of a virtual special issue on *Magnetic small-angle neutron scattering – from nanoscale magnetism to long-range magnetic structures*.

‡ Present address: Department of Physics, Indian Institute of Technology, Palakkad, Kerala, India.
§ Present address: Department of Physics and Astronomy, University of California Davis, Davis, CA 95616, USA.

Keywords: vortex lattices; MgB_2; small-angle neutron scattering; doping; structural transition.

Small-angle neutron scattering has been used to study the vortex lattice in superconducting MgB_2 doped with either manganese or carbon to achieve a similar suppression of the critical temperature. Measurements were performed with the magnetic field applied along the *c* axis, where the vortex lattice in pure MgB_2 is known to undergo a field- and temperature-driven 30° rotation transition. For Mn doping, the vortex lattice phase diagram remains qualitatively similar to that of pure MgB_2, indicating only a modest effect on the vortex–vortex interaction. In contrast, the vortex lattice rotation transition is completely suppressed in the C-doped case, probably due to a change in the electronic structure which affects the two-band/two-gap nature of superconductivity in MgB_2. The vortex lattice longitudinal correlation length shows the opposite behavior, remaining roughly unchanged between pure and C-doped MgB_2 while it is significantly reduced in the Mn-doped case. However, the extensive vortex lattice metastability and related activated behavior, observed in conjunction with the vortex lattice transition in pure MgB_2, are also seen in the Mn-doped sample. This shows that the vortex lattice disordering is not associated with a substantially increased vortex pinning.

1. Introduction

Vortex matter in type-II superconductors is highly sensitive to the environment provided by the host material. As an example, one can consider the vortex lattice (VL) symmetry, orientation and even transitions between different orientations, which are governed by anisotropies in the screening current plane perpendicular to the applied field and the associated non-local vortex–vortex interactions (Kogan *et al.*, 1997*a*,*b*; Franz *et al.*, 1997; Agterberg, 1998; Ichioka *et al.*, 1999). As no material is perfectly isotropic, the observation of anisotropy effects in superconductors is near ubiquitous, with examples given in our recent review on magnetic small-angle neutron scattering (SANS) (Mühlbauer *et al.*, 2019). The VL may also be used to probe the superconducting state itself, as demonstrated by the recent evidence for broken time-reversal symmetry in the topological superconductor UPt_3 (Avers *et al.*, 2020). Here we focus on how the VL in MgB_2 is affected by both non-magnetic and magnetic doping.

The VL phase diagram in MgB_2 with **H** ∥ **a** consists of three different VL phases, shown later in Fig. 4(*a*). All the VL phases have a triangular symmetry, differing only in their orientation relative to the crystalline axes (Cubitt *et al.*, 2003; Das *et al.*, 2012). In the F and I phases, the VL is oriented along

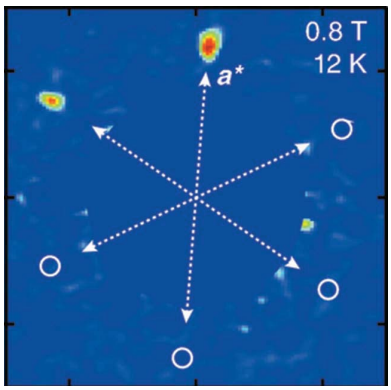

the crystalline a- and a^*-axis directions, respectively. In the intermediate L phase, the VL undergoes a continuous 30° rotation transition between these two high-symmetry directions within the hexagonal crystalline basal plane. The VL rotation is due to the field- and temperature-dependent supercarrier density within the π and σ bands in MgB_2, resulting in a change of the relative strength of their competing anisotropies (Zhitomirsky & Dao, 2004; Hirano *et al.*, 2013; Olszewski *et al.*, 2020). The VL phase diagram can be tuned by rotating the applied field away from the c axis, which first suppresses and eventually eliminates the intermediate L phase, and leads to a discontinuous transition between the F and I phases (Leishman *et al.*, 2021).

In addition to a rich phase diagram, the VL in MgB_2 displays extensive metatstability upon cooling or heating across the equilibrium phase boundaries, attributed to the presence of VL domain boundaries (Das *et al.*, 2012; Rastovski *et al.*, 2013). Recent studies of the transition kinetics, using vortex motion to gradually drive a supercooled VL from the metastable to the equilibrium state, allowed a determination of the associated activation barrier (Louden *et al.*, 2019*b*,*c*). Here, the activation barrier was found to increase as the metastable state is suppressed, corresponding to an aging of the VL.

To further explore how the vortex–vortex interaction in MgB_2 can be modified, we have used SANS to study samples doped with either magnetic manganese (Mn) or non-magnetic carbon (C) atoms on the Mg and B sites, respectively. Here, doping levels were chosen to achieve roughly the same suppression of the critical temperature (T_c). In the Mn-doped case, the VL phase diagram remained largely the same as that for pure MgB_2, although a clear disordering was observed through a decrease in the longitudinal VL correlation length. Conversely, the C-doped sample demonstrated a complete suppression of the L phase, while the correlation length remained unaffected compared with pure MgB_2. Finally, VL metastability and activated behavior was still observed in the Mn-doped sample, although with a slightly higher activation barrier compared with pure MgB_2.

2. Crystal growth and characterization

Single crystals of $Mg(B_{1-x}C_x)_2$ and $(Mg_{1-x}Mn_x)B_2$ were grown by a high-pressure flux method from an excess solution of magnesium (Karpinski *et al.*, 2003; Mou *et al.*, 2016; Taufour, 2021). Elemental Mg, B, and dopant Mn or C were packed inside a 1 cm diameter boron nitride (BN) crucible in the ratio of Mg:B:(Mn/C) = 1:0.7:x. The dopant C/Mn was placed at the bottom of the crucibles for maximum incorporation within the Mg melt, and above it a pressed Mg pellet and B powder were placed. The crucible was tightly packed with BN powder to prevent any Mg leakage at high pressure and temperature. To reduce neutron absorption during the SANS experiments, isotopically pure ^{11}B was used for the growth. However, due to contamination from the BN crucibles and powder made with natural boron, the MgB_2 crystals contain ∼5% neutron absorbing ^{10}B (Cubitt *et al.*, 2003). Using a cubic anvil furnace, a pressure of 3.5 GPa was applied to the crucible at room temperature, and it was then heated to 1430 °C and held at this temperature for 1 h. Afterwards, the temperature was decreased to the melting point of Mg (650 °C) over a period of 6 h. After completion of the crystal growth, the furnace heating was turned off to achieve a faster cooling and the pressure was released. This procedure yields MgB_2 single crystals embedded inside the solidified Mg melt. Individual single crystals were extracted by distilling the excess Mg at 750 °C inside an evacuated quartz tube. The crystals for the SANS experiments had a flat-plate morphology, with side lengths of roughly half a millimetre and masses in the 50–100 µg range.

For the SANS measurements, C- and Mn-doped crystals were chosen to have roughly equal T_c, determined from zero-field-cooled magnetization measurements. For the selected $Mg(B_{1-x}C_x)_2$ crystals, $T \approx 34$ K, indicating a dopant concentration of $x = 0.04$–0.07 (Wilke *et al.*, 2004, 2007; Kazakov *et al.*, 2005). For the $(Mg_{1-x}Mn_x)B_2$ crystals, $T \approx 33$ K, corresponding to a doping of $x = 0.005 \pm 0.001$ (Rogacki *et al.*, 2006). Field-temperature phase diagrams for both the carbon- and the manganese-doped samples are shown in Fig. 1. Linear fits to the upper critical field [$H_{c2}(T)$] near the T_c for $\mathbf{H} \parallel \mathbf{c}$ yields slopes of $dH_{c2}/dT = -0.22$ T K^{-1} and -0.090 T K^{-1} for the C- and Mn-doped samples, respectively. Also shown for

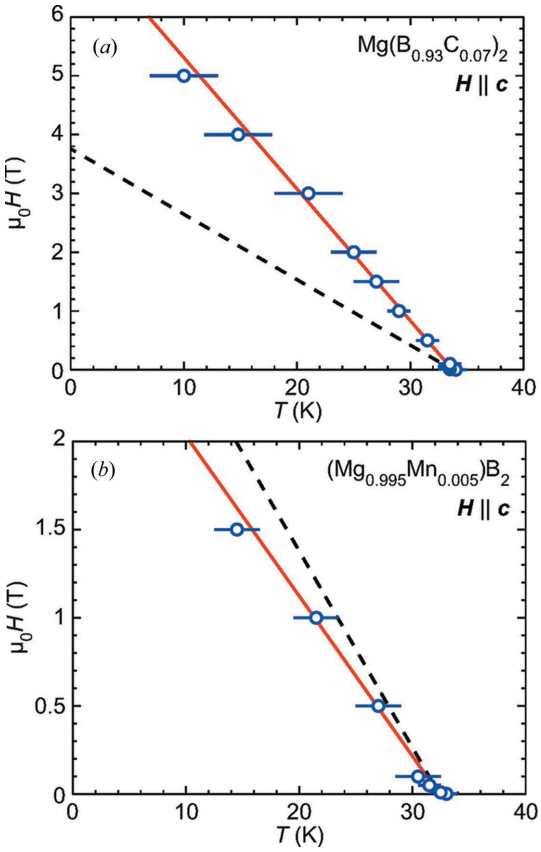

Figure 1
Temperature dependence of the upper critical field obtained from magnetization measurements for (*a*) $Mg(B_{0.93}C_{0.07})_2$ and (*b*) $(Mg_{0.995}Mn_{0.005})B_2$. The solid lines are linear fits to $H_{c2}(T)$ close to T_c. The dashed lines show $H_{c2}(T)$ for pure $Mg^{11}B_2$ (Das *et al.*, 2012), but shifted along the temperature axis to vanish at T_c for the doped samples.

comparison is $dH_{c2}/dT = -0.11$ T K^{-1} for pure $Mg^{11}B_2$ (Das *et al.*, 2012). Consistent with earlier reports, the slope for $(Mg_{0.995}Mn_{0.005})B_2$ is roughly the same as for undoped MgB_2 (Rogacki *et al.*, 2006), while it doubled for $Mg(B_{0.93}C_{0.07})_2$ (Kazakov *et al.*, 2005; Angst *et al.*, 2005).

3. Small-angle neutron scattering

The SANS measurements were performed using a conventional geometry for VL studies with the applied field parallel to the incident neutron beam (Mühlbauer *et al.*, 2019). Experiments were carried out at the D33 beamline at the Institut Laue–Langevin (Eskildsen *et al.*, 2016), the GP-SANS beamline at Oak Ridge National Laboratory (ORNL) (Heller *et al.*, 2018) and the NG7 beamline at the NIST Center for Neutron Research (NCNR). The crystal orientations were verified using a back-scattering X-ray Laue camera system (Multiwire Laboratories Ltd) at the ORNL Spallation Neutron Source X-ray laboratory.

The magnetic field was applied parallel to the crystalline c axis, and the sample and magnet were rotated together to satisfy the Bragg condition for the VL with scattering angles given by $\sin\theta_0 \approx \theta_0 = Q_{VL}\lambda_n/4\pi$ (Mühlbauer *et al.*, 2019). Here

$$Q_{VL} = 2\pi\sqrt{2B/\sqrt{3}\Phi_0}$$

is the magnitude of the scattering vector for a triangular VL, $\Phi_0 = h/2e = 2068$ T nm^2 is the superconducting flux quantum, and λ_n is the neutron wavelength.

The magnetic induction B is equal to the applied field $\mu_0 H$ as the magnetization for our samples is negligible at the fields used in the SANS experiments. Diffracted neutrons were collected on a 2D position sensitive detector.

The SANS measurements were performed at temperatures between $T = 2$ K and $T = 20$ K, and magnetic fields in the range $\mu_0 H = 0.3$–2.5 T. For the determination of the equilibrium phase diagram, the VL was prepared at each field and temperature by applying a damped field oscillation, which is known to produce well-ordered equilibrium VL states in pure MgB_2 (Rastovski *et al.*, 2013). Studies of non-equilibrium VLs and the metastable-to-equilibrium transition kinetics were preceded by cooling across the F–L phase transition in a constant field to render the VL in a metastable state (Das *et al.*, 2012). Subsequently, the VL was gradually driven from the metastable F phase to the equilibrium L phase by successive application of a.c. magnetic field oscillations with an amplitude of 0.93 mT and a frequency of 250 Hz (Louden *et al.*, 2019*b*,*c*). Here, the a.c. field is parallel to the d.c. field.

4. Results

The results of our SANS measurements related to the equilibrium VL phase diagram, the structural ordering of the VL and the metastable-to-equilibrium transition kinetics are presented in the following.

4.1. Equilibrium VL phase diagram

As already discussed, the equilibrium VL phase diagram in pure MgB_2, shown in Fig. 4(*a*) (see below), consists of three different triangular phases (Das *et al.*, 2012): an F phase with Bragg peaks along the crystalline a-axis direction, an I phase with peaks along the a^*-axis direction and an intermediate L phase where the VL undergoes a continuous 30° rotation transition. In the F and I phases, where the VL is oriented along one of the high-symmetry crystalline directions, the SANS diffraction patterns show six Bragg peaks. In contrast, in the L phase, there is a twofold degeneracy with respect to the direction of the VL rotation (clockwise versus counterclockwise), leading to the presence of oppositely rotated domains and six pairs of azimuthally split Bragg peaks. Fig. 2 shows representative SANS diffraction patterns obtained for $Mg(B_{0.93}C_{0.07})_2$ and $(Mg_{0.995}Mn_{0.005})B_2$. To conserve beamtime, not all VL peaks were rocked through the Bragg condition; however, their positions can be determined by successive 60° rotations around the origin of reciprocal space ($Q = 0$), as indicated by the circles. In the case of carbon doping, an F phase VL, shown in Fig. 2(*a*), is observed at all the fields and temperatures where it was possible to image the VL by SANS. In contrast, all three VL phases are observed for the manganese-doped sample, as illustrated in Figs. 2(*b*)–2(*d*).

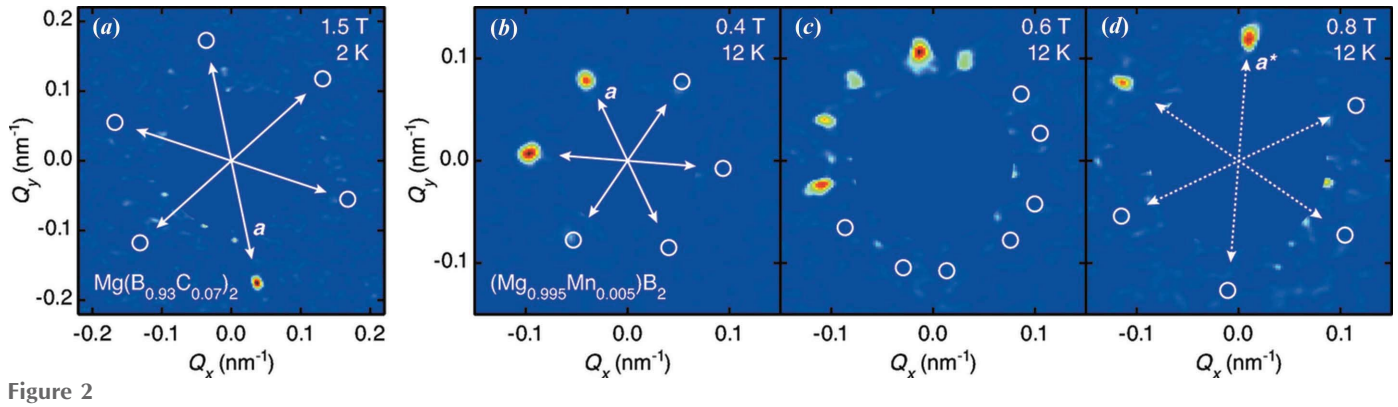

Figure 2
Diffraction patterns illustrating the observed VL phases. (*a*) The F phase in $Mg(B_{0.93}C_{0.07})_2$. The (*b*) F, (*c*) L and (*d*) I phases in $(Mg_{0.995}Mn_{0.005})B_2$. Background scattering is subtracted and a portion of reciprocal space close to $Q = 0$ is masked off. Crystalline axes in the hexagonal basal plane are indicated by arrows and the positions of symmetry-related VL peaks that were not brought into the Bragg condition are indicated by circles.

In undoped MgB_2, thermal fluctuations are insufficient to overcome the activation barrier required for transitions between the F, L and I phases, giving rise to extensive metastability (Louden *et al.*, 2019*c*). However, an equilibrium VL configuration may be achieved at any given field and temperature by introducing vortex motion, for example, through the application of a damped field oscillation (Das *et al.*, 2012). This is also the case for $(Mg_{0.995}Mn_{0.005})B_2$, as evident from the comparison between different field and temperature histories in Fig. 3, showing the VL scattered intensity versus the azimuthal angle (φ) for one 60° segment of the diffraction pattern. Here, the reference direction φ_0 is along the *a* axis, such that a single peak at $\varphi = \varphi_0$ corresponds to the F phase, whereas split peaks around φ_0 correspond to the L phase. As seen in Fig. 3(*a*), field cooling from $T > T_c$ results in a majority F phase VL. The smaller shoulders on the main peaks indicate the presence of minor L phase domains. In contrast, an L phase VL is obtained either by cooling in a high field followed by a field reduction, as shown in Fig. 3(*c*), or following a zero field cooling and a subsequent field application at base temperature, as shown in Fig. 3(*b*). In both cases, significant vortex motion was induced by the field change. Applying a damped field oscillation, with an initial amplitude of 75 mT, causes a transition from the VL F phase shown in Fig. 3(*a*) to an L phase shown in Fig. 3(*d*). This confirms that the F phase is metastable, while the L phase is the equilibrium VL configuration at the specific field and temperature. This is consistent with the results in Figs. 3(*e*) and 3(*f*). Here, the additional vortex motion induced by the damped field oscillation only gives rise to slight changes in the population of the two domain orientations, as indicated by the relative intensity of the peaks, while the VL remains in the L phase with an unchanged peak splitting $\Delta\varphi \approx 22°$.

The equilibrium VL phase diagrams are summarized in Figs. 4(*b*) and 4(*c*) for $Mg(B_{0.93}C_{0.07})_2$ and $(Mg_{0.995}Mn_{0.005})B_2$, respectively, with that for undoped MgB_2 shown in Fig. 4(*a*) for comparison. At each field and temperature measured, a damped field oscillation with an initial amplitude of 50 mT was applied before imaging the VL to ensure an equilibrium configuration. Symbols indicate where SANS imaging of the VL was performed, with the limiting factor being the vanishing scattering intensity at both high temperatures and fields. In particular, even a modest extension along the field axis would require excessive count times due to the exponential decrease of the intensity. For the carbon-doped sample, only the F phase is observed, as seen in Fig. 4(*b*), although other VL phases may exist at high fields and/or temperatures. That said, the measurements extended up to 2.5 T $\approx 0.44H_{c2}$, which is an order of magnitude higher than the F–L transition observed in undoped MgB_2, both on an absolute (0.2 T) and on a relative scale ($\sim 0.06H_{c2}$). The VL phase diagram for $Mg(B_{0.93}C_{0.07})_2$ thus appears to be qualitatively different from that of pure MgB_2. In comparison, the phase diagram for $(Mg_{0.995}Mn_{0.005})B_2$, shown in Fig. 4(*c*), only differs quantitatively from that of undoped MgB_2. Specifically, the F–L phase boundary has moved to higher fields and the

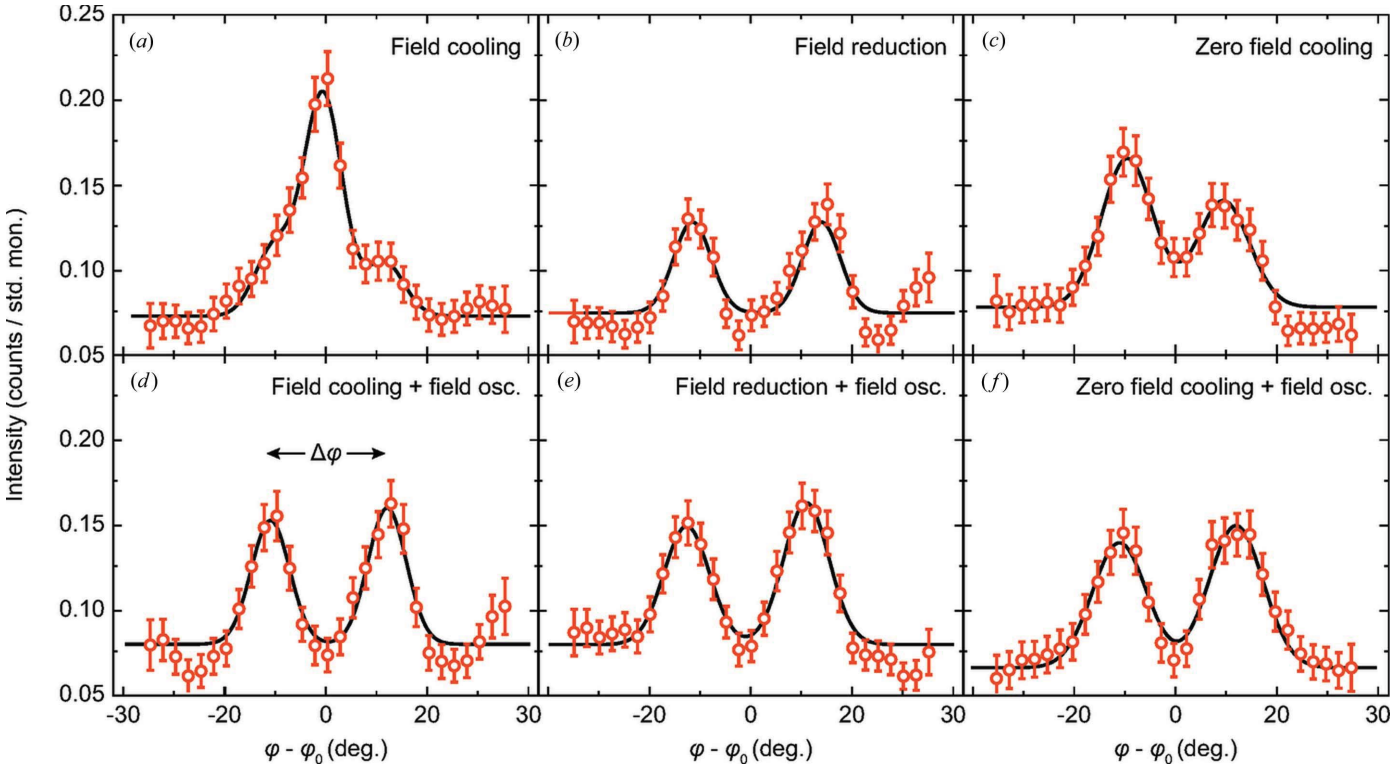

Figure 3
Azimuthal VL intensity distribution for $(Mg_{0.995}Mn_{0.005})B_2$ at 0.45 T and 2.1 K, following different field and temperature histories. The top panels correspond to (*a*) field cooling, (*b*) field reduction from 4 T and (*c*) zero field cooling. In the bottom panels (*d*)–(*f*), the above field histories were followed by a damped field oscillation. The solid lines are multi-Gaussian fits. The VL Bragg peak splitting $\Delta\varphi$ is indicated in panel (*d*).

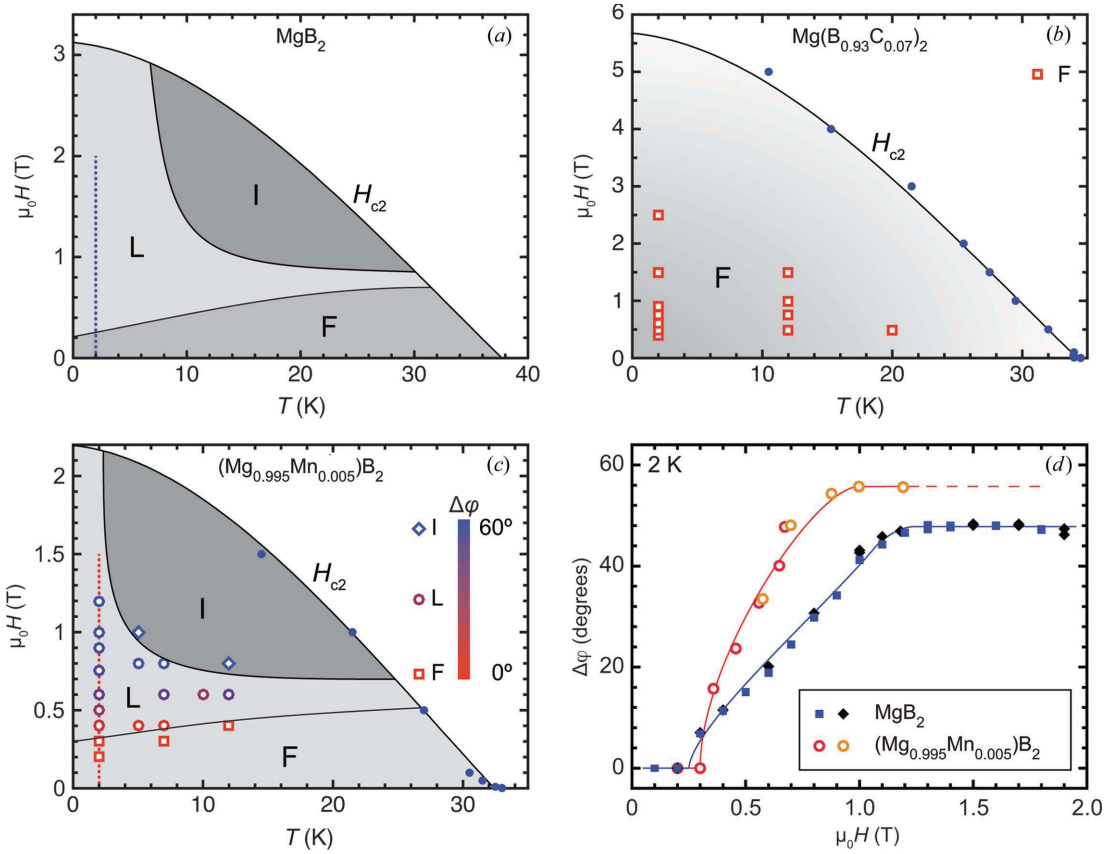

Figure 4
VL phase diagrams: (*a*) MgB_2 (Das *et al.*, 2012), (*b*) $Mg(B_{0.93}C_{0.07})_2$ and (*c*) $(Mg_{0.995}Mn_{0.005})B_2$. In panels (*b*) and (*c*), the upper critical fields are based on the data in Fig. 1 and extrapolated to $T = 0$, and vertical dotted lines indicate the field-sweeps in panel (*d*). In (*c*), the color of the data points reflects the VL Bragg peak splitting $\Delta\varphi$, with 0 and 60° corresponding to the F and I phases, respectively. (*d*) Comparison of the field dependence of the VL Bragg peak splitting at 2 K for pure (Das *et al.*, 2012) and Mn-doped MgB_2. Errors on the peak splitting do not exceed the size of the symbols. Blue/red and black/orange symbols correspond to increasing and decreasing fields, respectively. All lines are guides for the eye.

L–I boundary has shifted to lower temperatures, resulting in a shrinking of the L phase. As seen in Fig. 4(*d*), the VL peak splitting angle $\Delta\varphi$, determined from multi-peak Gaussian fits to the azimuthal intensity distribution, saturates at the highest measured fields. This suggests that the L phase in $(Mg_{0.995}Mn_{0.005})B_2$ extends to the upper critical field at low temperature, similar to the situation in undoped MgB_2. Still, the low-temperature saturation angle $\Delta\varphi \approx 56°$ is closer to the value of the I phase (60°) than to the value for the pure compound (∼44°).

4.2. Longitudinal correlation length

Both lattice imperfections and the finite experimental resolution cause the VL reflections to broaden in reciprocal

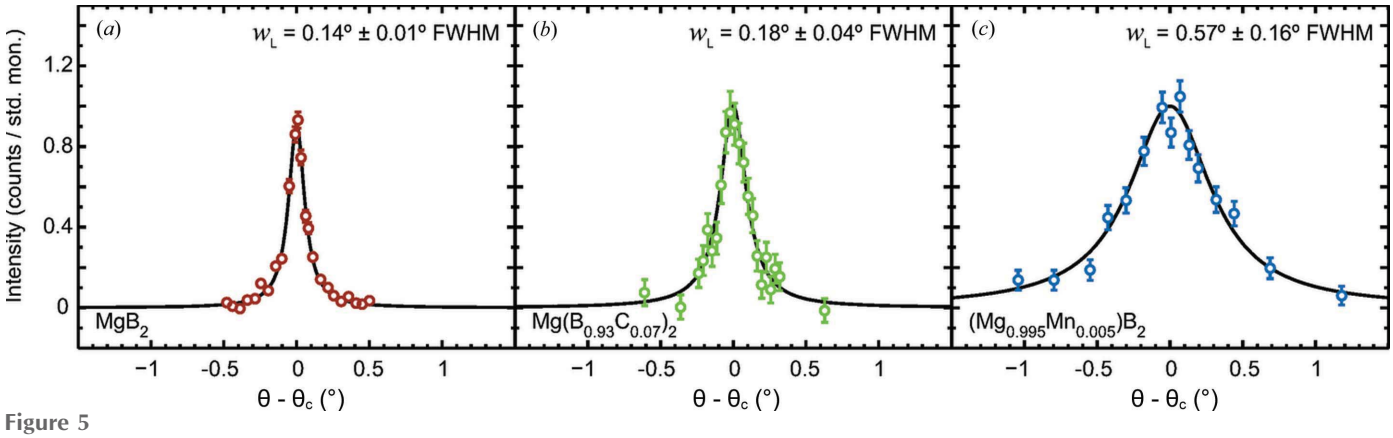

Figure 5
VL rocking curves for (*a*) MgB_2, (*b*) $Mg(B_{0.93}C_{0.07})_2$ and (*c*) $(Mg_{0.995}Mn_{0.005})B_2$. All measurements were performed at 0.5 T and 2 K. Solid lines are Voigt fits to the data as discussed in the text, with Lorentzian widths indicated in the individual panels.

space, with scattering occurring for a range of angles around the Bragg condition. Fig. 5 shows the scattered intensity as the VL is rotated through the Bragg condition at $\theta = \theta_0$ in a typical 'rocking curve' for both pure and doped MgB_2. While the rocking curve for $Mg(B_{0.93}C_{0.07})_2$ only shows a slight broadening compared with the undoped compound, that of $(Mg_{0.995}Mn_{0.005})B_2$ is substantially wider.

Spatial correlations for the VL are expected to decay exponentially with distance, which, in the absence of experimental broadening, leads to rocking curves with a Lorentzian line shape. This allows a determination of the longitudinal correlation length (*i.e.* along the field direction),

$$\zeta_L = \frac{d_0}{\pi w_L}, \tag{1}$$

where $d_0 = \sqrt{2\Phi_0/\sqrt{3}B}$ is the vortex separation (69 nm at 0.5 T) and w_L is the Lorentzian FWHM in radians. In situations where the intrinsic broadening is comparable to the instrumental resolution, rocking curves are best described by a Voigt profile:

$$V(\theta) = \int_{-\infty}^{\infty} G(\theta')\, L(\theta - \theta')\, \mathrm{d}\theta'. \tag{2}$$

This is a convolution of the Lorentzian (L) representing the intrinsic width and a Gaussian (G) determined by the experimental resolution (Eskildsen, 1998; Louden *et al.*, 2019*a*). The curves in Fig. 5 are Voigt fits to the data. In all cases, the Gaussian width, estimated from the neutron wavelength, wavelength spread and beam collimation used in the respective SANS experiment (Eskildsen, 1998), was kept fixed during the fitting. Compared with the rather poor experimental resolution within the detector plane evident from Fig. 3, the perpendicular Gaussian width is reduced by a factor $(Q_{VL}\lambda_n)/2\pi \sim 10^{-2}$ (Mühlbauer *et al.*, 2019). For the present measurements, the Lorentzian width dominated the experimental resolution, allowing a precise determination of ω_L and thus the longitudinal correlation length. From the Lorentzian widths, listed in each panel of Fig. 5, we find $\zeta_L \approx 9$ µm for undoped MgB_2, $\zeta_L \approx 7$ µm for $Mg(B_{0.93}C_{0.07})_2$ and $\zeta_L \approx 2$ µm for $(Mg_{0.995}Mn_{0.005})B_2$. Note that while the rocking curves for the doped samples were measured during the same SANS experiment, and are thus directly comparable, that for the pure compound was obtained separately. A comparison between $Mg(B_{0.93}C_{0.07})_2$ and MgB_2 may therefore be affected by systematic errors, and their correlation lengths should be considered equivalent.

4.3. Metastable-to-equilibrium state transition kinetics

The presence of robust metastable states makes it possible to study the VL transition kinetics and determine the activation barrier separating the metastable and equilibrium states in $(Mg_{0.995}Mn_{0.005})B_2$, using the same stop-motion technique as for undoped MgB_2 (Louden *et al.*, 2019*b*,*c*). First, a pristine metastable F phase VL is prepared by applying a damped field oscillation at 0.5 T and 25 K, and then cooling the sample across the F–L phase boundary to a final temperature of 2 K. A measurement sequence is then performed, alternating between SANS imaging of the VL and applications of small-amplitude a.c. magnetic field cycles. The latter introduces a modest amount of vortex motion which gradually drives the VL towards the equilibrium state.

The results of the measurement sequence are summarized in Fig. 6. Panel (*a*) shows an example of the the azimuthal intensity distribution, with scattering from both the metastable

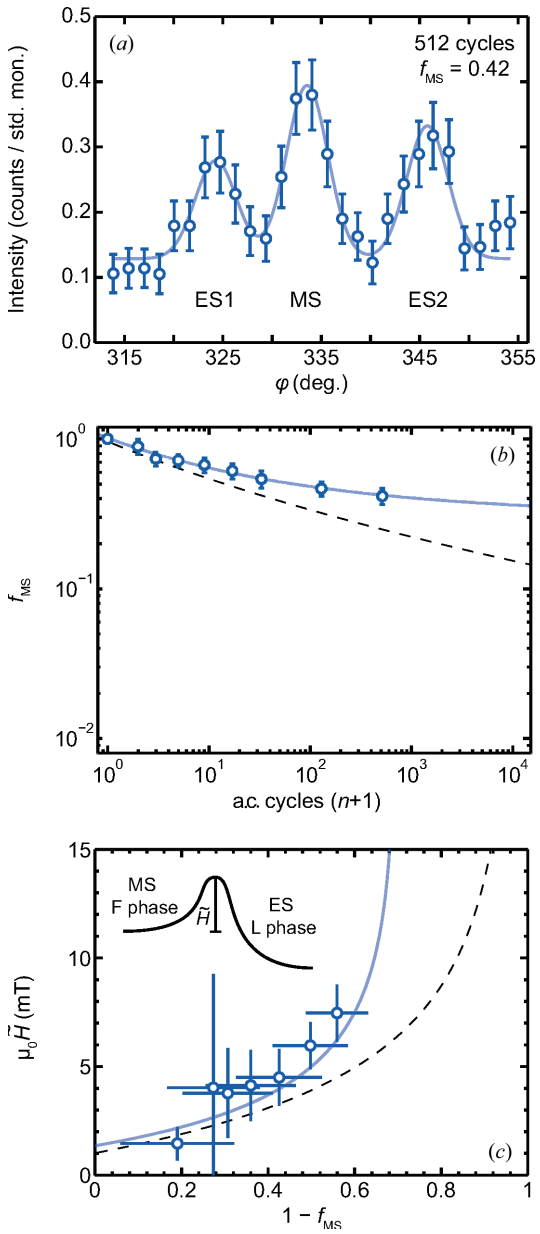

Figure 6
VL transtion kinetics for $(Mg_{0.995}Mn_{0.005})B_2$ for a 0.93 mT a.c. field amplitude with a frequency of 250 Hz. (*a*) Azimuthal intensity distribution after 512 field cycles fitted to three Gaussians of the same width. (*b*) Metastable VL volume fraction versus the number of applied a.c. field cycles. The cycle count is offset by one such that $f_{MS}(0)$ may be included, and the solid line is a fit to equation (6). (*c*) The activation field determined from $f_{MS}(n)$ using equation (5). The solid line is calculated using the parameters obtained from the fit in panel (*b*). The dashed lines in panels (*b*) and (*c*) are for pure MgB_2, and the same a.c. field amplitude and frequency (Louden *et al.*, 2019*c*).

F phase (MS) and the equilibrium L phase (ES1/ES2) domains clearly evident. The population of each domain orientation is proportional to the corresponding peak intensity, determined from a three-Gaussian fit, and the volume fraction remaining in the metastable state is thus given by

$$f_{\rm MS} = \frac{I_{\rm MS}}{I_{\rm ES1} + I_{\rm MS} + I_{\rm ES2}}. \quad (3)$$

Here, the width used for the Gaussian fits is determined from the pristine metastable F phase (0 cycles) and then kept fixed (Louden *et al.*, 2019*c*). The evolution of $f_{\rm MS}$ as a function of the cumulative a.c. field cycle count (n) is shown in Fig. 6(*b*).

Assuming an activated behavior, with the a.c. field amplitude ($H_{\rm ac}$) and n taking the roles of, respectively, an effective 'temperature' and 'time', the evolution of the metastable volume fraction is given by (Louden *et al.*, 2019*c*)

$$\frac{{\rm d}f_{\rm MS}}{{\rm d}n} = -f_{\rm MS} \exp(-\tilde{H}/H_{\rm ac}). \quad (4)$$

The activation field $\tilde{H}$, representing the barrier between the metastable and equilibrium VL domain orientations, is determined experimentally from adjacent values of $f_{\rm MS}(n)$ by

$$\tilde{H} = -H_{\rm ac} \ln\left\{-\frac{\ln[f_{\rm MS}(n_{i+1})/f_{\rm MS}(n_i)]}{n_{i+1} - n_i}\right\} \quad (5)$$

and shown in Fig. 6(*c*). The increasing $\tilde{H}(n)$ is equivalent to an aging of the VL (Henkel & Pleimling, 2010).

Similar to pure MgB_2, the metastable volume fraction for the Mn-doped sample in Fig. 6(*b*) is well fitted by (Louden *et al.*, 2019*c*)

$$f_{\rm MS}(n) = \exp[\alpha + \beta(n+1)^{\gamma}]. \quad (6)$$

Here, $\beta \approx -\alpha$ is introduced to accommodate a value of $f_{\rm MS}(0)$ slightly less than one. From the fitted values of α and γ, one obtains two physical quantities (Louden *et al.*, 2019*c*). First, $\alpha_{\rm Mn} \approx \frac{1}{3}\alpha_{\rm pure}$ yields a roughly one order of magnitude increase in the saturation value $f_{\rm MS}(n \to \infty) = e^{\alpha}$ [vertical asymptote of the fits in Fig. 6(*c*)]. Second, α and β combined allows a calculation of the initial value of the activation barrier $\tilde{H}(f_{\rm MS} = 1)$, which remains largely unchanged compared with pure MgB_2.

5. Discussion

The SANS studies of the VL phase diagrams in doped MgB_2 furthers our understanding of the superconducting properties of this material. Theoretically, it was found that the stability of the VL F and I phases may be attributed to the Fermi surface anisotropy of the π and σ bands, respectively (Hirano *et al.*, 2013). Combined with the suppression of π-band superconductivity by an applied field (Eskildsen *et al.*, 2002), this leads to the observed VL phase diagram (Cubitt *et al.*, 2003; Das *et al.*, 2012). The $F \to L \to I \to L$ phase sequence along H_{c2} from T_c to zero temperature remains a robust feature upon variations of both the intra- and interband pairing constants, as long as none of them vanish (Hirano *et al.*, 2013). However, the relative fraction of the phase diagram occupied by the different states will change depending on the gap ratio Δ_π/Δ_σ. Setting both the σ-band pairing and the interband coupling equal to zero completely eliminates the I phase and substantially reduces the range of stability of the L phase. This picture, combined with results from previous experimental studies of MgB_2 doped with either carbon or manganese, is consistent with our SANS results, as shall be discussed in the following.

Between the two dopants studied, Mn affects the superconductivity in MgB_2 in the simplest manner. Within the explored doping range, T_c and $H_{c2}(0)$ for $\mathbf{H} \parallel \mathbf{c}$ are both suppressed while maintaining a linear relationship, and ${\rm d}H_{c2}/{\rm d}T$ at the critical temperature remains unaffected (Rogacki *et al.*, 2006). This implies minimal changes in the intraband scattering for both the π and σ bands. Furthermore, point contact spectroscopy shows that the distinct superconducting gaps for the π and σ bands are preserved up to the highest achievable doping levels (T_c = 10 K), and interband scattering must therefore remain weak (Gonnelli *et al.*, 2006). The conclusion of these studies is that Mn doping predominantly influences the superconducting properties through spin-flip scattering, with the reduction of T_c being due to magnetic pair breaking. This is consistent with our observation of a VL phase diagram which is qualitatively similar to that of pure MgB_2. At the quantitative level, the gap ratio Δ_π/Δ_σ increases slightly with Mn doping (Gonnelli *et al.*, 2006), which is predicted to increase the range of stability of the F and L phases, and decrease the I phase (Hirano *et al.*, 2013). In contrast, we observe an increase of both the F and I phases at the expense of the L phase, as seen in Figs. 4(*a*) and 4(*c*). This suggests that either the simple model of Hirano *et al.* does not fully capture the behavior of the VL in MgB_2 or that the slightly increased intraband scattering due to the Mn doping changes the effective range of the non-local vortex–vortex interaction and slightly shifts the phase boundaries. We will return to the second possibility later.

In the case of C doping, the effect on the superconducting properties is more complex (Gurevich, 2003; Wilke *et al.*, 2004; Kortus *et al.*, 2005*a*,*b*; Samuely *et al.*, 2005*b*). As was the case for Mn doping, point contact spectroscopy studies found a modest reduction of Δ_σ, while Δ_π remained largely unaffected for C-doping concentrations comparable to that in studies by SANS (Gonnelli *et al.*, 2005; Samuely *et al.*, 2005*a*; Szabó *et al.*, 2007). In the absence of other effects, one would therefore expect only minor modifications of the VL phase diagram, in analogy with the Mn-doped case. Therefore, the complete suppression of the L and I phases clearly demonstrates the presence of additional effects. Theoretically, the lack of a doping dependence for Δ_π and Δ_σ, the reduction of T_c, and the increase of both $H_{c2}(0)$ and ${\rm d}H_{c2}/{\rm d}T$ is explained by the compensating effects of increased intra- and interband scattering and a reduction of the σ-band density of states due to the electron doping by carbon (Kortus *et al.*, 2005*a*,*b*; Samuely *et al.*, 2005*b*; Angst *et al.*, 2005; Kazakov *et al.*, 2005; Wilke *et al.*, 2007). Experimentally, this is also found to increase the resilience of the π-band superconductivity to magnetic fields (Szabó *et al.*, 2007). Both the reduction of the σ-band density

of states and the increased robustness of the π-band superconductivity will favor the VL F phase at the expense of the L and I phases (Hirano *et al.*, 2013), consistent with our SANS results.

We now return to the discussion of potential modifications to the VL phase diagram due to a reduction of the mean free path, and by extension the range of the non-local vortex–vortex interactions. To put this in context, consider the triangular-to-square VL symmetry transition observed in most superconductors with a fourfold basal plane anisotropy (Mühlbauer *et al.*, 2019). This transition is driven solely by a change of the vortex density and occurs when the separation is a certain fraction of the nonlocality range (Kogan *et al.*, 1997*a*,*b*). As shown for $Lu(Ni_{1-x}Co_x)_2B_2C$, the symmetry transition is shifted to progressively higher fields as the mean free path is reduced with increasing Co doping (Gammel *et al.*, 1999). In contrast, the rotation between the F and I phases in MgB_2 is driven by the suppression of the π-band superconductivity with increasing field, rather than the accompanying change of the vortex density. While the slight change of the VL phase diagram in Mn-doped MgB_2 may be due to a reduced mean free path, it is unlikely to explain the complete suppression of the L and I phases in the C-doped case. Rather, one would expect the opposite effect, as C doping has been found to enhance the π-band intraband scattering more rapidly than that of the σ-band (Szabó *et al.*, 2007), which will suppress the influence of the π-band Fermi surface anisotropy and thus disfavor the VL F phase.

Finally, we comment on the structural properties of the VL together with the metastability and transition kinetics in Mn-doped MgB_2. While the longitudinal correlation length is considerably decreased compared with the pure and C-doped samples, as indicated by the broadening rocking curves seen in Fig. 5(*c*), clear VL Bragg peaks are still observed on the SANS detector, as shown in Figs. 2(*b*)–2(*d*). That said, some in-plane broadening is observed relative to the C-doped sample, as shown in Fig. 2(*a*). However, due to the poor in-plane resolution, a quantitative comparison is not feasible as the peak widths for both pure and C-doped MgB_2 are resolution limited. We note that a substantial rocking curve broadening is observed in other materials that include magnetic elements, such as $ErNi_2B_2C$ (Yaron *et al.*, 1996) and $TmNi_2B_2C$ (Eskildsen, 1998), regardless of whether the magnetic moments order. At this time, this is simply an observation for which we do not have a clear explanation. The decreased correlation length in the Mn-doped sample is probably not indicative of substantially increased vortex pinning. This notion is supported by the azimuthal widths in Fig. 3, which show no field history dependence. For materials with low-to-moderate pinning, field oscillations will either leave the VL unchanged or give rise to a further ordering, as seen, for example, in YNi_2B_2C (Levett *et al.*, 2002). In contrast, in materials with strong pinning, the least disordered VL is, in our experience, obtained by a field cooling, and any subsequent fields changes will lead to additional disordering. A final argument against strong pinning comes from the transition kinetics summarized in Fig. 6. This shows that it is still possible to induce vortex motion and drive the VL from the metastable to the equilibrium state by small amplitude field oscillations. At the qualitative level, Mn-doped MgB_2 again shows the same behavior as the pure compound, although there are quantitative differences in the saturation value $f_{MS}(n \rightarrow \infty)$.

6. Conclusions

We have studied the VL in MgB_2 that has been doped with either manganese or carbon. While only minor changes to the phase diagram were observed in the Mn-doped case, a single VL phase is observed for C doping within the range of fields and temperatures explored. This is consistent with the current understanding of superconductivity in MgB_2. The VL metastability previously observed in pure MgB_2 is also seen for the Mn-doped case despite a significant reduction of the longitudinal correlation length.

Acknowledgements

We thank J. Barker for help with the SANS experiments as NCNR and T. Williams for assistance collecting the X-ray Laue data. Ames Laboratory is operated for the US Department of Energy by Iowa State University. We acknowledge the support of the National Institute of Standards and Technology, US Department of Commerce, in providing the neutron research facilities used in this work. A portion of this research used resources at the High Flux Isotope Reactor and at the Spallation Neutron Source X-ray laboratory, DOE Office of Science User Facilities operated by the Oak Ridge National Laboratory.

Funding information

Funding for the neutron scattering was provided by the US Department of Energy, Office of Basic Energy Sciences (award No. DE-SC0005051). SM was funded by the Gordon and Betty Moore Foundations EPiQS Initiative (grant No. GBMF4411). The work at Ames was supported by the US Department of Energy, Office of Science, Basic Energy Sciences, Materials Science and Engineering Division (contract No. AC02-07CH11358).

References

Agterberg, D. F. (1998). *Phys. Rev. B*, **58**, 14484–14489.
Angst, M., Bud'ko, S. L., Wilke, R. H. T. & Canfield, P. C. (2005). *Phys. Rev. B*, **71**, 144512.
Avers, K. E., Gannon, W. J., Kuhn, S. J., Halperin, W. P., Sauls, J. A., DeBeer-Schmitt, L., Dewhurst, C. D., Gavilano, J., Nagy, G., Gasser, U. & Eskildsen, M. R. (2020). *Nat. Phys.* **16**, 531–535.
Cubitt, R., Eskildsen, M. R., Dewhurst, C. D., Jun, J., Kazakov, S. M. & Karpinski, J. (2003). *Phys. Rev. Lett.* **91**, 047002.
Das, P., Rastovski, C., O'Brien, T. R., Schlesinger, K. J., Dewhurst, C. D., DeBeer-Schmitt, L., Zhigadlo, N. D., Karpinski, J. & Eskildsen, M. R. (2012). *Phys. Rev. Lett.* **108**, 167001.
Eskildsen, M. R. (1998). PhD thesis, University of Copenhagen, Denmark. http://www.risoe.dk/rispubl/FYS/ris-r-1084.htm.
Eskildsen, M. R., Archer, J., De Waard, E., Dewhurst, C., Honecker, D. & White, J. (2016). *Tuning the vortex lattice metastability in*

MgB2 by non-magnetic and magnetic doping. Institut Laue–Langevin, https://doi.ill.fr/10.5291/ILL-DATA.5-42-420.
Eskildsen, M. R., Kugler, M., Tanaka, S., Jun, J., Kazakov, S. M., Karpinski, J. & Fischer, Ø. (2002). *Phys. Rev. Lett.* **89**, 187003.
Franz, M., Affleck, I. & Amin, M. (1997). *Phys. Rev. Lett.* **79**, 1555–1558.
Gammel, P. L., Bishop, D. J., Eskildsen, M. R., Mortensen, K., Andsersen, N. H., Fisher, I. R., Cheon, K. O., Canfield, P. C. & Kogan, V. G. (1999). *Phys. Rev. Lett.* **82**, 4082–4085.
Gonnelli, R., Daghero, D., Ummarino, G. A., Calzolari, A., Tortello, M., Stepanov, V. A., Zhigadlo, N. D., Rogacki, K., Karpinski, J., Bernardini, F. & Massidda, S. (2006). *Phys. Rev. Lett.* **97**, 037001.
Gonnelli, R. S., Daghero, D., Calzolari, A., Ummarino, G. A., Dellarocca, V., Stepanov, V. A., Kazakov, S. M., Zhigadlo, N. D. & Karpinski, J. (2005). *Phys. Rev. B*, **71**, 060503.
Gurevich, A. (2003). *Phys. Rev. B*, **67**, 184515.
Heller, W. T., Cuneo, M., Debeer-Schmitt, L., Do, C., He, L., Heroux, L., Littrell, K., Pingali, S. V., Qian, S., Stanley, C., Urban, V. S., Wu, B. & Bras, W. (2018). *J. Appl. Cryst.* **51**, 242–248.
Henkel, M. & Pleimling, M. (2010). *Non-Equilibrium Phase Transitions*, Vol. 2, *Ageing and Dynamical Scaling Far from Equilibrium*. Berlin: Springer.
Hirano, T., Takamori, K., Ichioka, M. & Machida, K. (2013). *J. Phys. Soc. Jpn*, **82**, 063708.
Ichioka, M., Hasegawa, A. & Machida, K. (1999). *Phys. Rev. B*, **59**, 8902–8916.
Karpinski, J., Angst, M., Jun, J., Kazakov, S. M., Puzniak, R., Wisniewski, A., Roos, J., Keller, H., Perucchi, A., Degiorgi, L., Eskildsen, M. R., Bordet, P., Vinnikov, L. & Mironov, A. (2003). *Supercond. Sci. Technol.* **16**, 221–230.
Kazakov, S. M., Puzniak, R., Rogacki, K., Mironov, A. V., Zhigadlo, N. D., Jun, J., Soltmann, C., Batlogg, B. & Karpinski, J. (2005). *Phys. Rev. B*, **71**, 024533.
Kogan, V. G., Bullock, M., Harmon, B., Miranović, P., Dobrosavljević-Grujić, L., Gammel, P. L. & Bishop, D. J. (1997*a*). *Phys. Rev. B*, **55**, R8693–R8696.
Kogan, V. G., Miranović, P., Dobrosavljević-Grujić, L., Pickett, W. E. & Christen, D. K. (1997*b*). *Phys. Rev. Lett.* **79**, 741–744.
Kortus, J., Dolgov, O. V., Kremer, R. K. & Golubov, A. A. (2005*a*). *Phys. Rev. Lett.* **94**, 027002.
Kortus, J., Dolgov, O. V., Kremer, R. K. & Golubov, A. A. (2005*b*). *Phys. Rev. Lett.* **95**, 099702.
Leishman, A. W. D., Sokolova, A., Bleuel, M., Zhigadlo, N. D. & Eskildsen, M. R. (2021). *Phys. Rev. B*, **103**, 094516.
Levett, S. J., Dewhurst, C. D. & Paul, D. M. (2002). *Phys. Rev. B*, **66**, 014515.
Louden, E. R., Leishman, A. W. D., Rastovski, C., Kuhn, S. J., DeBeer-Schmitt, L., Dewhurst, C. D., Zhigadlo, N. D. & Eskildsen, M. R. (2019*a*). *New J. Phys.* **21**, 063003.
Louden, E. R., Rastovski, C., DeBeer-Schmitt, L., Dewhurst, C. D., Zhigadlo, N. D. & Eskildsen, M. R. (2019*b*). *Phys. Rev. B*, **99**, 144515.
Louden, E. R., Rastovski, C., Kuhn, S. J., Leishman, A. W. D., DeBeer-Schmitt, L., Dewhurst, C. D., Zhigadlo, N. D. & Eskildsen, M. R. (2019*c*). *Phys. Rev. B*, **99**, 060502.
Mou, D., Manni, S., Taufour, V., Wu, Y., Huang, L., Bud'ko, S. L., Canfield, P. C. & Kaminski, A. (2016). *Phys. Rev. B*, **93**, 144504.
Mühlbauer, S., Honecker, D., Périgo, A., Bergner, F., Disch, S., Heinemann, A., Erokhin, S., Berkov, D., Leighton, C., Eskildsen, M. R. & Michels, A. (2019). *Rev. Mod. Phys.* **91**, 015004.
Olszewski, M. W., Eskildsen, M. R., Reichhardt, C. & Reichhardt, C. J. O. (2020). *Phys. Rev. B*, **101**, 224504.
Rastovski, C., Schlesinger, K. J., Gannon, W. J., Dewhurst, C. D., DeBeer-Schmitt, L., Zhigadlo, N. D., Karpinski, J. & Eskildsen, M. R. (2013). *Phys. Rev. Lett.* **111**, 107002.
Rogacki, K., Batlogg, B., Karpinski, J., Zhigadlo, N. D., Schuck, G., Kazakov, S. M., Wägli, P., Puzniak, R., Wisniewski, A., Carbone, F., Brinkman, A. & van der Marel, D. (2006). *Phys. Rev. B*, **73**, 174520.
Samuely, P., Hoľanová, Z., Szabó, P., Wilke, H. T., Bud'ko, S. L. & Canfield, P. C. (2005*a*). *Phys. Status Solidi (C)*, **2**, 1743–1748.
Samuely, P., Szabó, P., Canfield, P. C. & Bud'ko, S. L. (2005*b*). *Phys. Rev. Lett.* **95**, 099701.
Szabó, P., Samuely, P., Pribulová, Z., Angst, M., Bud'ko, S., Canfield, P. C. & Marcus, J. (2007). *Phys. Rev. B*, **75**, 144507.
Taufour, V. (2021). *Fundamentals of Quantum Materials*, edited by J. Paglione, N. P. Butch & E. E. Rodriguez, ch. 10, pp. 221–237. Singapore: World Scientific.
Wilke, R. H. T., Bud'ko, S. L., Canfield, P. C., Finnemore, D. K., Suplinskas, R. J. & Hannahs, S. T. (2004). *Phys. Rev. Lett.* **92**, 217003.
Wilke, R. H. T., Samuely, P., Szabó, P., Hoľanová, Z., Bud'ko, S. L., Canfield, P. C. & Finnemore, D. K. (2007). *Physica C*, **456**, 108–116.
Yaron, U., Gammel, P. L., Ramirez, A. P., Huse, D. A., Bishop, D. J., Goldman, A. I., Stassis, C., Canfield, P. C., Mortensen, K. & Eskildsen, M. R. (1996). *Nature*, **382**, 236–238.
Zhitomirsky, M. E. & Dao, V. H. (2004). *Phys. Rev. B*, **69**, 054508.